GEOPHYSICS, VOL. 65, NO. 5 (SEPTEMBER-OCTOBER 2000); P. 1527–1541, 13 FIGS., 2 TABLES.

3-D ground-penetrating radar simulation and plane-wave theory in anisotropic media

José M. Carcione* and Michael A. Schoenberg‡

ABSTRACT

Modeling ground-penetrating radar (GPR) waves requires simulation of the 3-D full wavefield and the correct description of the electromagnetic (EM) properties. Magnetic and dielectric relaxations are described by relaxation functions associated with each principal component of the respective tensorial property. Anisotropy is modeled up to orthorhombic symmetry, i.e., the principal coordinate systems of the three EM material tensors coincide, and each property is described by three different principal components.

The algorithm uses the pseudospectral method for computing the spatial derivatives and a second-order finite difference in time. A complete plane-wave analysis, including energy balance, gives the expressions of measurable quantities such as the EM-wave velocity and the quality factor as a function of frequency and propagation direction. The algorithm reproduces the wavefront shape and attenuation predicted by the plane-wave analysis. In addition, the results are in excellent agreement with an analytical 3-D transient solution. The modeling is applied to evaluation of the EM response of two pipes buried in an anisotropic sand overlying a clay layer. The results demonstrate that anisotropy and loss mechanisms cause significant amplitude and phase distortions.

INTRODUCTION

The increasing use of ground-penetrating radar (GPR) for solving a wide range of engineering and environmental problems has been facilitated by the application of standard seismic techniques, such as multifold coverage and processing (e.g., Fisher et al., 1992; Pipan et al., 1996). Some attempts have been made to apply 3-D seismic techniques to the interpretation of radar signals (Hu, 1992; Grandjean and Gourry, 1996; Grasmueck, 1996). For 3-D surveys over complicated geology or objects, it is not simple to determine the origin of all recorded arrivals. In this sense, 3-D modeling is useful for interpreting radar profiles, evaluating 3-D processing techniques, and, in general, understanding wave propagation in complex electromagnetic (EM) media.

To date, 3-D full-wave modeling applied to GPR studies has been rather scarce. Wang and Tripp (1994) and Roberts and Daniels (1997) use a finite-difference time-domain method (FDTD) to model GPR data in isotropic conducting media. The latter authors also model antenna characteristics. Schneider and Hudson (1993) develop an FDTD algorithm for general anisotropic materials, assuming frequency-independent permittivity and conductivity properties.

It is well known from laboratory and field data that it is essential to model dissipation effects (for most rocks, electromagnetic Q is lower lower than seismic Q). Moreover, anisotropy and variations in magnetic permeability were recently observed in field experiments (Tillard, 1994; Walker, 1997). Anisotropy may be found at different scales (Negi and Saraf, 1989); finely stratified layers, compaction, fluid-filled cracks, and fractures give rise to anisotropy in electric and magnetic properties. Since the dielectric constant of water is 80 and that for most dry rocks is 4–8, a set of aligned, fluid-filled fractures may present a high degree of dielectric anisotropy. Similarly, the presence of mineralized water (high ionic conductivity) in the fractures produces anisotropy in the electrical conductivity. In some cases, such as interbedded shales and sandstones, the longitudinal conductivity can be as much as nine times the transverse conductivity. Moreover, in most crystalline solids such as rocks and ice, intrinsic anisotropy occurs because of the preferred arrangement of the atoms and molecules. These facts indicate that the interpretation of GPR data is becoming more complicated; therefore, we need a suitable modeling tool to tackle these problems.

In 3-D space, the Fourier method (Reshef et al., 1988a,b) appears suitable for computing spatial derivatives since it requires a smaller number of grid points than finite-difference techniques to achieve the same accuracy. Use of the Fourier method for 2-D GPR forward modeling is recent. Zeng et al. (1995) and Casper and Kung (1996) implement the standard

Manuscript received by the Editor June 11, 1998; revised manuscript received January 13, 2000.
*Osservatorio Geofisico Sperimentale, P.O. Box 2011 Opicina, 34016 Trieste, Italy. E-mail: jcarcione@ogs.trieste.it.
‡Schlumberger-Doll Research, Ridgefield, Connecticut 06877-4108. E-mail: mike@ridgefield.sdr.slb.com.

seismic version developed by Kosloff and Baysal (1982) for modeling waves in lossy media with ohmic conductivity losses. Carcione (1996a,b) solves Maxwell's equations for lossy media, including dielectric relaxation processes and out-of-phase electric currents. The technique is based on the introduction of memory or hidden variables (Carcione et al., 1988). The same approach is used by Xu and McMechan (1997) for solving Maxwell's differential equations in 2.5 dimensions.

In this paper, we use the same modeling scheme implemented by Reshef et al. (1988a,b) and Carcione et al. (1992) for computing the spatial derivatives and a staggered second-order time integration technique. Moreover, the constitutive equations include anisotropy and dissipation caused by different magnetic, dielectric, and electric processes. As mentioned, anisotropy can be intrinsic or effective, and dissipation can be caused by many dielectric relaxation mechanisms (see Hasted, 1973, p. 238), ionic conductivity, and, in some soils, ferromagnetic-domain relaxation and superparamagnetic relaxation (Olhoeft and Capron, 1994).

From the numerical and physical views, 3-D modeling is similar to the 2-D version described in Carcione (1996c), with the addition of magnetic relaxation processes—that is, the inclusion of a time-dependent magnetic permeability tensor. By using the acoustic-electromagnetic analogy, a set of standard linear solid elements describes several magnetic and dielectric relaxation mechanisms, and a single Kelvin-Voigt element incorporates the out-of-phase behavior of the electric conductivity (any deviation from Ohm's law). The use of a set of elements allows the fitting of any arbitrary dependence of the velocity and quality factor versus frequency. We assume the media are orthorhombic, i.e., the principal systems of the three material tensors coincide and a different relaxation function is associated with each principal component. The physics of wave propagation is illustrated by probing the medium with a uniform plane wave. The present analysis gives the expressions of measurable quantities, such as energy velocity and quality factor, as a function of propagation direction and frequency.

MAXWELL'S EQUATIONS FOR GENERAL ANISOTROPIC MEDIA

In 3-D vector notation, Maxwell's equations are (e.g., Chew, 1990)

$$\nabla \times \mathbf{E} = -\frac{\partial \mathbf{B}}{\partial t} + \mathbf{M}_s$$

and (1)

$$\nabla \times \mathbf{H} = \frac{\partial \mathbf{D}}{\partial t} + \mathbf{J},$$

where the vectors $\mathbf{E}$, $\mathbf{H}$, $\mathbf{D}$, $\mathbf{B}$, $\mathbf{J}$, and $\mathbf{M}_s$ are the electric field intensity, the magnetic field intensity, the electric flux density, the magnetic flux density, the electric current density (including an electric source current), and the magnetic source current densities, respectively. In general, they depend on the Cartesian coordinates (x_1, x_2, x_3) and the time variable t. Additional constitutive relations are needed to relate fluxes to the field intensities. For lossless anisotropic media, the electric current density consists entirely of a source term, $\mathbf{J}_s$. The constitutive equations are $\mathbf{D} = \boldsymbol{\epsilon} \cdot \mathbf{E}$ and $\mathbf{B} = \boldsymbol{\mu} \cdot \mathbf{H}$, where $\boldsymbol{\epsilon}$, the dielectric permittivity tensor, and $\boldsymbol{\mu}$, the magnetic permeability tensor, are real, symmetric, positive definite tensors (e.g., the scalar product between $\mathbf{H}$ and $\mathbf{B}$ is greater than or equal to zero) and the dot denotes ordinary matrix multiplication. The relation $\mathbf{D} = \boldsymbol{\epsilon} \cdot \mathbf{E}$ can be written as (Carcione, 1996c)

$$\mathbf{D}(t) = \boldsymbol{\epsilon} \cdot \int_{-\infty}^{\infty} \delta(t-\tau)\mathbf{E}(\tau)\, d\tau = \boldsymbol{\epsilon} \cdot \int_{-\infty}^{\infty} H(t-\tau)\frac{\partial \mathbf{E}(\tau)}{\partial t} d\tau \equiv \boldsymbol{\epsilon} * \frac{\partial \mathbf{E}}{\partial t},$$

where the asterisk implies time convolution in the dot product sense.

For anisotropic lossy media including dielectric relaxation and magnetic loss, $\mathbf{D}$ and $\mathbf{B}$ can be written as

$$\mathbf{D} = \boldsymbol{\epsilon} * \frac{\partial \mathbf{E}}{\partial t}$$

and (2)

$$\mathbf{B} = \boldsymbol{\mu} * \frac{\partial \mathbf{H}}{\partial t},$$

where $\boldsymbol{\epsilon}(\mathbf{x}, t)$ is the time-dependent dielectric permittivity tensor and $\boldsymbol{\mu}(\mathbf{x}, t)$ is the time-dependent magnetic permeability tensor. The electric current density is given by the generalized Ohm's law,

$$\mathbf{J} = \boldsymbol{\sigma} * \frac{\partial \mathbf{E}}{\partial t} + \mathbf{J}_s, \tag{3}$$

where $\boldsymbol{\sigma}(\mathbf{x}, t)$ is the time-dependent conductivity tensor, the convolution accounts for out-of-phase components of the conduction current density with respect to the electric field, and $\mathbf{J}_s$ is the electric source current density. Substituting the constitutive relations [equation (2)] and the current density [equation (3)] into equations (1) and using properties of the convolution gives

$$\nabla \times \mathbf{E} = -\boldsymbol{\mu} * \frac{\partial^2 \mathbf{H}}{\partial t^2} + \mathbf{M}_s$$

and (4)

$$\nabla \times \mathbf{H} = \boldsymbol{\sigma} * \frac{\partial \mathbf{E}}{\partial t} + \boldsymbol{\epsilon} * \frac{\partial^2 \mathbf{E}}{\partial t^2} + \mathbf{J}_s,$$

a system of six scalar equations in six scalar unknowns.

The time-dependent tensors, which are symmetric and positive definite, describe various EM relaxation processes of the material, such as dielectric relaxation and out-of-phase behavior of the conduction current at high frequencies. The time dependence is not arbitrary. Each tensor's eigenvectors are assumed invariant in time. So in a coordinate system coincident with these fixed eigenvectors, the time dependence of the tensor is fully specified by three time functions on the main diagonal, which serve as the time-dependent eigenvalues of the matrix. When the time dependence of the tensors is restricted to the Heaviside function, equations (4) reduce to Maxwell's equations for anisotropic media with no loss except that resulting from frequency-independent conductivity. These equations also include paramagnetic losses through the time-dependent permeability $\boldsymbol{\mu}$. Although the magnetic permeability is commonly assumed to be that of free space, some soils have a significantly higher value because of ferromagnetic domain relaxation and superparamagnetic relaxation (Olhoeft and Capron, 1994).

ELECTROMAGNETIC EQUATIONS FOR ORTHORHOMBIC MEDIA

In general, each of the symmetric and positive definite tensors $\boldsymbol{\mu}$, $\boldsymbol{\epsilon}$, and $\boldsymbol{\sigma}$ has a set of mutually perpendicular

eigenvectors. If there is no eigenvector in common for all three tensors, the medium is said to be triclinic. If there is a single eigenvector common to all three tensors, the medium is said to be monoclinic and has a mirror plane of symmetry perpendicular to the common eigenvector.

In this work, we are concerned with orthorhombic media for which $\boldsymbol{\mu}$, $\boldsymbol{\epsilon}$, and $\boldsymbol{\sigma}$ have coincident eigenvectors. Rotating to a coordinate system defined by those common eigenvectors allows the tensors to be written as

$$\boldsymbol{\mu} = \begin{pmatrix} \mu_1 & 0 & 0 \\ 0 & \mu_2 & 0 \\ 0 & 0 & \mu_3 \end{pmatrix}, \qquad \boldsymbol{\epsilon} = \begin{pmatrix} \epsilon_1 & 0 & 0 \\ 0 & \epsilon_2 & 0 \\ 0 & 0 & \epsilon_3 \end{pmatrix}, \qquad \boldsymbol{\sigma} = \begin{pmatrix} \sigma_1 & 0 & 0 \\ 0 & \sigma_2 & 0 \\ 0 & 0 & \sigma_3 \end{pmatrix}. \tag{5}$$

The following symmetries are embraced by the term orthotropy:

1) *orthorhombic*, for which there are no two eigendirections for which all three tensors have equal eigenvalues;
2) *transverse isotropy*, for which there are two and only two eigendirections for which all three tensors have equal eigenvalues, e.g., if the two directions are the 1- and 2-directions, then $\mu_1 = \mu_2$, $\epsilon_1 = \epsilon_2$, and $\sigma_1 = \sigma_2$; this EM symmetry includes that of hexagonal, tetragonal, and trigonal crystals; and
3) *isotropy*, for which all three tensors have three equal eigenvalues, i.e., they are all isotropic tensors; crystals of cubic symmetry are electromagnetically isotropic.

We show below that a medium is orthorhombic if the dispersion relation is a function of the squares of the components of the slowness vector.

For the sake of simplicity in evaluating the final equations, we consider a Cartesian system that coincides with the principal system of the medium. For brevity, the general equations are not given, but the method for obtaining them can be found in Carcione (1996c). The EM equations (4) in Cartesian components are

$$\begin{aligned}
\frac{\partial E_2}{\partial x_3} - \frac{\partial E_3}{\partial x_2} &= \mu_1 * \frac{\partial^2 H_1}{\partial t^2} + M_1, \\
\frac{\partial E_3}{\partial x_1} - \frac{\partial E_1}{\partial x_3} &= \mu_2 * \frac{\partial^2 H_2}{\partial t^2} + M_2, \\
\frac{\partial E_1}{\partial x_2} - \frac{\partial E_2}{\partial x_1} &= \mu_3 * \frac{\partial^2 H_3}{\partial t^2} + M_3, \\
\frac{\partial H_3}{\partial x_2} - \frac{\partial H_2}{\partial x_3} &= \sigma_1 * \frac{\partial E_1}{\partial t} + \epsilon_1 * \frac{\partial^2 E_1}{\partial t^2} + J_1, \\
\frac{\partial H_1}{\partial x_3} - \frac{\partial H_3}{\partial x_1} &= \sigma_2 * \frac{\partial E_2}{\partial t} + \epsilon_2 * \frac{\partial^2 E_2}{\partial t^2} + J_2,
\end{aligned} \tag{6}$$

and

$$\frac{\partial H_2}{\partial x_1} - \frac{\partial H_1}{\partial x_2} = \sigma_3 * \frac{\partial E_3}{\partial t} + \epsilon_3 * \frac{\partial^2 E_3}{\partial t^2} + J_3.$$

Form of the tensor components

A realistic description of dielectric and magnetic relaxation can be obtained by representing the principal components with a generalized Debye model. This model accounts for many relaxation mechanisms.

The principal components of the dielectric tensor can be expressed as

$$\epsilon_i(t) = \epsilon_i^0 \left[1 - \frac{1}{L_i} \sum_{\ell=1}^{L_i} \left(1 - \frac{\lambda_{i\ell}}{\tau_{i\ell}} \right) \exp(-t/\tau_{i\ell}) \right] H(t), \qquad i = 1, \ldots, 3, \tag{7}$$

where ϵ_i^0 is the static permittivity, $\lambda_{i\ell}$ and $\tau_{i\ell}$ are relaxation times ($\lambda_{i\ell} \le \tau_{i\ell}$), L_i is the number of Debye relaxation mechanisms, and $H(t)$ is the Heaviside function. The condition $\lambda_{i\ell} \le \tau_{i\ell}$ makes the relaxation function (7) analogous to the viscoelastic creep function of standard linear solid elements connected in series (e.g., Casula and Carcione, 1992). The optical (or high-frequency) permittivity

$$\epsilon_i^\infty = \frac{\epsilon_i^0}{L_i} \sum_{\ell=1}^{L_i} \frac{\lambda_{i\ell}}{\tau_{i\ell}} \tag{8}$$

is obtained as $t \to 0$. Note that $\epsilon_i^\infty \le \epsilon_i^0$ always.

Similarly, the principal components of the permeability tensor can be written as

$$\mu_i(t) = \mu_i^0 \left[1 - \frac{1}{N_i} \sum_{n=1}^{N_i} \left(1 - \frac{\gamma_{in}}{\theta_{in}} \right) \exp(-t/\theta_{in}) \right] H(t), \qquad n = 1, \ldots, 3, \tag{9}$$

where μ_i^0 is the static permeability, $\gamma_{i\ell}$ and $\theta_{i\ell}$ are relaxation times ($\gamma_{i\ell} \le \theta_{i\ell}$), and N_i is the number of Debye relaxation mechanisms.

On the other hand, the conductivity components are represented by a Kelvin-Voigt mechanical model analog (e.g., Casula and Carcione, 1992):

$$\sigma_i(t) = \sigma_i^0 [H(t) + \chi_i \delta(t)], \qquad i = 1, \ldots 3, \tag{10}$$

where σ_i^0 is the static conductivity, χ_i is a relaxation time, and $\delta(t)$ is the Dirac function. The out-of-phase component of the conduction current is quantified by the relaxation time χ_i. As shown later, this choice implies a component of the conduction current 90° out of phase with respect to the electric field.

Electromagnetic equations in differential form

Equations (6) could be the basis for a numerical solution algorithm. However, the numerical evaluation of the convolution integrals is prohibitive when solving the differential equations with grid methods and explicit time evolution techniques. The conductivity terms pose no problems, since conductivity does not involve time convolution. To circumvent the convolutions in the permittivity and permeability components, a new set of field variables is introduced, following the same approach as in two dimensions (Carcione, 1996c).

The dielectric hidden variables are defined as

$$e_{i\ell} = -\frac{1}{\tau_{i\ell}} \phi_{i\ell} * E_i, \qquad l = 1, \ldots, L_i, \tag{11}$$

where $i = 1, 2$, and 3, respectively, and

$$\phi_{i\ell}(t) = \frac{H(t)}{L_i \tau_{i\ell}}\left(1 - \frac{\lambda_{i\ell}}{\tau_{i\ell}}\right)\exp(-t/\tau_{i\ell}), \qquad l = 1, \ldots, L_i. \tag{12}$$

The hidden variables are the time derivatives of the polarization variables introduced by Petropoulos (1995) to model several relaxation processes of the Debye type.

Similarly, the magnetic hidden variables are

$$d_{in} = -\frac{1}{\theta_{in}}\varphi_{in} * H_i, \qquad l = 1, \ldots, N_i, \tag{13}$$

where

$$\varphi_{in}(t) = \frac{H(t)}{N_i \theta_{in}}\left(1 - \frac{\gamma_{in}}{\theta_{in}}\right)\exp(-t/\theta_{in}), \qquad n = 1, \ldots, N_i. \tag{14}$$

Following the same procedure as in two dimensions, the EM equations in differential form are

$$\begin{aligned}
\frac{\partial E_2}{\partial x_3} - \frac{\partial E_3}{\partial x_2} &= \mu_1^\infty \frac{\partial H_1}{\partial t} + \mu_1^0\left[\Psi_1 H_1 + \sum_{n=1}^{N_1} d_{1n}\right] + M_1,\\
\frac{\partial E_3}{\partial x_1} - \frac{\partial E_1}{\partial x_3} &= \mu_2^\infty \frac{\partial H_2}{\partial t} + \mu_2^0\left[\Psi_2 H_2 + \sum_{n=1}^{N_2} d_{2n}\right] + M_2,\\
\frac{\partial E_1}{\partial x_2} - \frac{\partial E_2}{\partial x_1} &= \mu_3^\infty \frac{\partial H_3}{\partial t} + \mu_3^0\left[\Psi_3 H_3 + \sum_{n=1}^{N_3} d_{3n}\right] + M_3,\\
\frac{\partial H_3}{\partial x_2} - \frac{\partial H_2}{\partial x_3} &= \sigma_{e1}^\infty E_1 + \epsilon_{e1}^\infty \frac{\partial E_1}{\partial t} + \epsilon_1^0 \sum_{\ell=1}^{L_1} e_{1\ell} + J_1,\\
\frac{\partial H_1}{\partial x_3} - \frac{\partial H_3}{\partial x_1} &= \sigma_{e2}^\infty E_2 + \epsilon_{e2}^\infty \frac{\partial E_2}{\partial t} + \epsilon_2^0 \sum_{\ell=1}^{L_2} e_{2\ell} + J_2,
\end{aligned} \tag{15}$$

and

$$\frac{\partial H_2}{\partial x_1} - \frac{\partial H_1}{\partial x_2} = \sigma_{e3}^\infty E_3 + \epsilon_{e3}^\infty \frac{\partial E_3}{\partial t} + \epsilon_3^0 \sum_{\ell=1}^{L_3} e_{3\ell} + J_3,$$

where

$$\epsilon_{ei}^\infty = \epsilon_i^\infty + \sigma_i^0 \chi_i \tag{16}$$

and

$$\sigma_{ei}^\infty = \sigma_i^0 + \epsilon_i^0 \Phi_i \tag{17}$$

are the effective optical permittivity and conductivity components, respectively, with

$$\Psi_i = \sum_{n=1}^{N_i} \varphi_{in}(0) \qquad \text{and} \qquad \Phi_i = \sum_{\ell=1}^{L_i} \phi_{i\ell}(0). \tag{18}$$

The first two terms on the right side of the last three of equations (15) correspond to the instantaneous response of the medium, as can be inferred from the relaxation functions (8) and (10). The terms containing the conductivity relaxation time χ_i are in phase with the instantaneous polarization response. The third terms in each equation involve the relaxation processes through the hidden variables.

The set of equations is completed with the differential equations corresponding to the hidden variables. Time differentiation of equations (11) and (13) and the use of convolution properties yield

$$\frac{\partial e_{i\ell}}{\partial t} = -\frac{1}{\tau_{i\ell}}[e_{i\ell} + \phi_{i\ell}(0)E_i]$$

and

$$\frac{\partial d_{in}}{\partial t} = -\frac{1}{\theta_{in}}[d_{in} + \varphi_{in}(0)H_i]. \tag{19}$$

Equations (15) and (19) give the EM response of a conducting anisotropic medium with magnetic and dielectric relaxation behavior and out-of-phase conduction currents. These equations are the basis of the numerical algorithm for obtaining the unknown vector field:

$$\mathbf{V} = [H_1, H_2, H_3, E_1, E_2, E_3, e_{i\ell}, d_{in}]^\top, \qquad \ell = 1, \ldots, L_i, \quad n = 1, \ldots, N_i. \tag{20}$$

The plane-wave theory is developed in Appendix A. This analysis gives the expressions of measurable quantities, such as slowness vector, energy velocity vector, and quality factor as a function of frequency.

SIMULATIONS

The radar equations can be written in compact matrix form as

$$\frac{\partial \mathbf{V}}{\partial t} = \mathbf{A}\mathbf{V} + \mathbf{S}, \tag{21}$$

where the unknown vector $\mathbf{V}$ is given by equation (20), matrix $\mathbf{A}$ contains the spatial derivatives and material properties, and $\mathbf{S}$ is a source vector.

Equation (21) is solved with a direct grid method, described in Appendix B. A modeling software package, 3DGEMS (Three-Dimensional Georadar Electromagnetic Modeling and Simulation), was developed to design the geological model, provide the kinematic and dynamic properties of each medium, and generate snapshots and radargrams.

Homogeneous medium

The material properties for a homogeneous medium are given in Table 1. Although the medium is not fully realistic (on the basis of known experimental data), its properties are chosen to illustrate the physics of wave propagation and to test the modeling code. Each permittivity and magnetic permeability component is associated with a single Debye relaxation, such that the respective relaxation times are given by

$$\lambda_i = \left(\tau_0/Q_i^\epsilon\right)\left(\sqrt{1 + Q_i^{\epsilon\,2}} - 1\right), \qquad \tau_i = \lambda_i + 2\left(\tau_0/Q_i^\epsilon\right)$$

and

$$\gamma_i = \left(\tau_0/Q_i^\mu\right)\left(\sqrt{1 + Q_i^{\mu\,2}} - 1\right), \qquad \theta_i = \gamma_i + 2\left(\tau_0/Q_i^\mu\right), \tag{22}$$

where $\tau_0 = 1/(2\pi f_0)$, with $f_0 = 550$ MHz, and Q_i^ϵ and Q_i^μ are the quality factors at f_0. Note that χ_i is inversely proportional to the respective static conductivity. The more dielectric the medium, the more the deviation from Ohm's law. As can be seen from equation (16), the relaxation time χ_i contributes to the effective optical permittivity, directly affecting the velocity.

Figure 1 shows sections of the energy velocity at the frequency f_0. The polarizations of the transverse magnetic (TM)

and transverse electric (TE) modes are indicated in the (x, y)-plane. Note that the electric field vector of the TM mode is not tangent to the wavefront curve. The quality factor curves [obtained from equation (A-47)] are represented in Figure 2 (the broken line corresponds to the TM mode), where (a) only includes the Debye relaxations and (b) also considers the contribution of the conductivity.

The numerical mesh used to solve equation (21) has $N_X = N_Y = N_Z = 117$ grid points per side, with a uniform grid spacing of 7.5 cm. This value satisfies the Nyquist criterion; thus, aliasing effects are avoided. The field is initiated by an electric current (such that $J_x = J_y = J_z$), with a central frequency of 550 MHz, and is propagated with a time step of 0.05 ns. We found, by trial simulations, that using a time step of $D_{\min}/(5v_{\max})$ gives stability and accuracy [if $D_{\min}$ is the minimum grid size and $v_{\max}$ is the maximum optical (high-frequency) velocity]. Figures 3, 4, and 5 contain snapshots of the magnetic and electric fields at the coordinate planes, computed at 130 ns. (The snapshots in Figure 5 are enhanced by a factor of 4 with respect to those of Figures 3 and 4.) They correspond to the lossless medium, the medium with dielectric and magnetic relaxations only, and the medium including all the losses, respectively. As

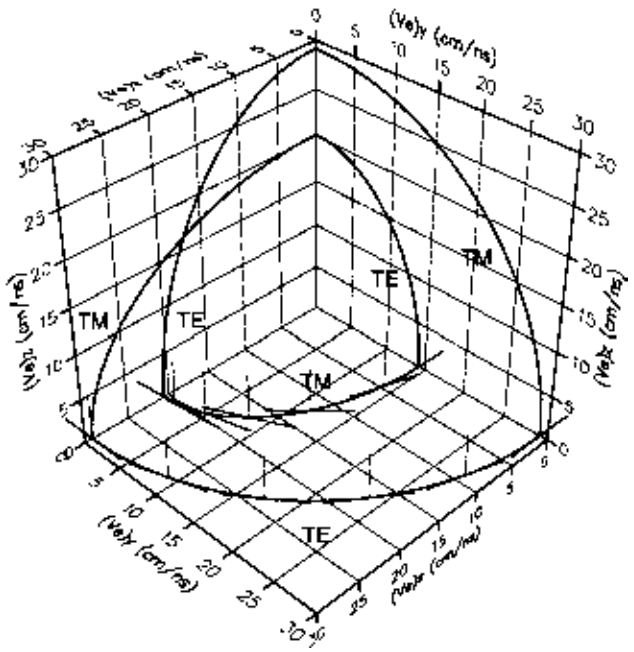

FIG. 1. Energy velocity (V_e) curves at the coordinate planes for a frequency of 550 MHz, where the TE and TM polarizations are indicated in the $(x$-$y)$-plane. The material properties are given in Table 1. Only one octant is shown from symmetry considerations.

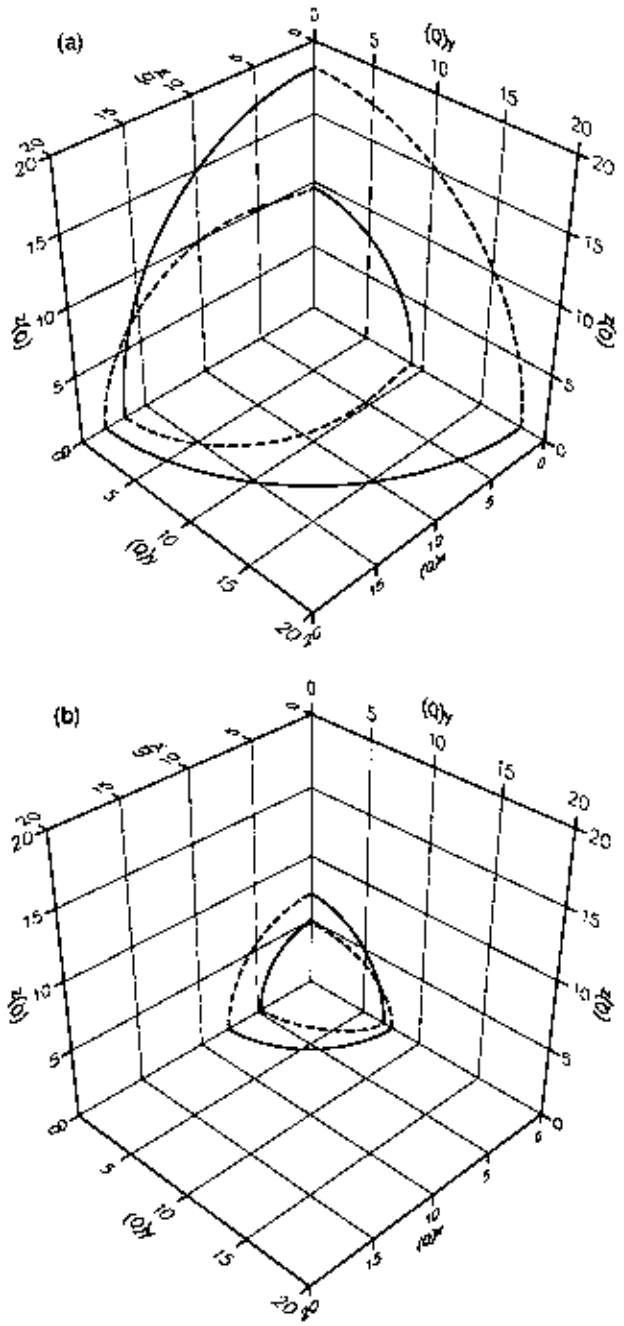

FIG. 2. Quality factor curves at the coordinate planes for a frequency of 550 MHz, with (a) corresponding to the Debye relaxation losses and (b) also including the conductivity losses. The dashed line is the TM mode, and the solid line is the TE mode. The material properties are given in Table 1. Only one octant is shown from symmetry considerations.

Table 1. Material properties.

ϵ_1^∞ (ϵ_0)	ϵ_2^∞ (ϵ_0)	ϵ_3^∞ (ϵ_0)	μ_1^∞ (μ_0)	μ_2^∞ (μ_0)	μ_3^∞ (μ_0)	σ_1^0 (S/m)	σ_2^0 (S/m)	σ_3^0 (S/m)
1	1	2	2	1	1	0.0025	0.005	0.0025
Q_1^ϵ	Q_2^ϵ	Q_3^ϵ	Q_1^μ	Q_2^μ	Q_3^μ	χ_1 (1/s)	χ_2 (1/s)	χ_3 (1/s)
10	20	20	200	200	100	$0.01\ \epsilon_0/\sigma_1^0$	$0.01\ \epsilon_0/\sigma_2^0$	$0.01\ \epsilon_0/\sigma_3^0$

$\epsilon_0 = 8.85\ 10^{-12}\ \mathrm{Fm}^{-1}$; $\mu_0 = 4\pi\ 10^{-7}\ \mathrm{Hm}^{-1}$

can be seen, the results of the simulations agree with the wave characteristics predicted by plane-wave analysis (see Figure 1). The features of the quality factors change substantially when including the conductivity losses (see Figure 2b). For instance, the TM mode in the (x, y)-plane and the TE mode in the (x, z)-plane (see Figure 5) are the most attenuated, in agreement with Figure 2b. Note the strong amplitude associated with the singularity in the (x, z)-plane.

An analytical solution for waves propagating in a 3-D lossy orthorhombic medium can be obtained when the electric permittivity tensor is proportional to the magnetic permeability tensor, i.e., $\boldsymbol{\mu} = a\boldsymbol{\epsilon}$, where a is the proportionality constant. For instance, the solution for the Green's function corresponding to the horizontal component of the magnetic field is

$$H_1 = \frac{1}{4\pi\rho^2}(x_3\bar{J}_2 - x_2\bar{J}_3)\left(\frac{1}{\rho} - i\omega\sqrt{\eta}\right)\exp(i\omega\rho\sqrt{\eta}), \tag{23}$$

where

$$\rho = \left(\frac{x_1^2}{\epsilon_1} + \frac{x_2^2}{\epsilon_2} + \frac{x_3^2}{\epsilon_3}\right)^{1/2}, \tag{24}$$

$\eta = a(\mu_0/\epsilon_0)\epsilon_2\epsilon_3$, with ϵ_i given in equation (A-12), and $\bar{J}_2$ and $\bar{J}_3$ the magnitudes of the electric-current components. We consider the medium defined in Table 1, with $a = 1$, i.e., $\mu_i^\infty = \epsilon_i^\infty$, $Q_i^\mu = Q_i^\epsilon$, for $i = 1, 2, 3$ and no conductivity losses. As before, the source is an electric current (such that $J_1 = J_2 = J_3$) with a central frequency of 550 MHz. The comparison between

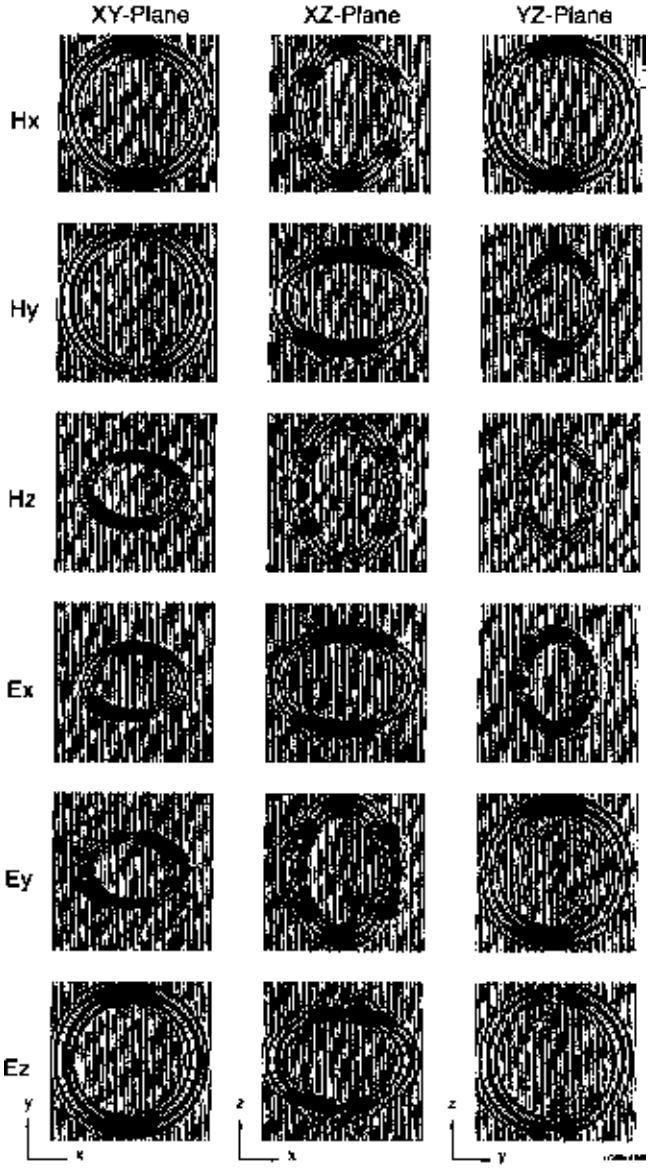

FIG. 3. Snapshots of the magnetic and electric fields at the coordinate planes (computed at 130 ns), corresponding to the lossless version of the the medium defined in Table 1.

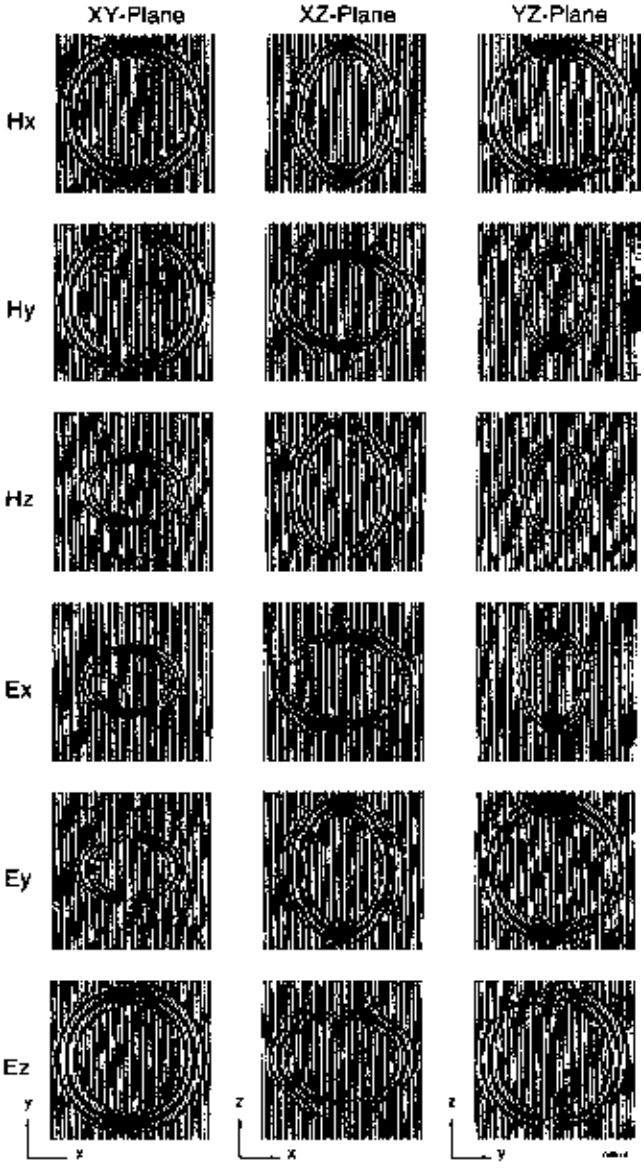

FIG. 4. Snapshots of the magnetic and electric fields at the coordinate planes (computed at 130 ns) for the medium defined in Table 1. The modeling includes dielectric and magnetic relaxations only.

the numerical and analytical solution is shown in Figure 6 for $x = 0.9$ m, $y = 0.9$ m, and $z = 1.35$ m. The agreement is very good.

Buried pipes in transversely isotropic sand

The second simulation considers two pipes in contact—one metal, the other plastic—buried in a lossy transversely isotropic (TI) sand layer. The model is displayed in Figure 7, and the material properties are listed in Table 2; the magnetic permeability is assumed to be that of vacuum and $\chi_i = 0$, for $i = 1, \ldots, 3$. The dielectric relaxation and TI properties of the sand result from the assumption that it is saturated with water and has a finely laminated structure, respectively. Figure 8 shows the energy velocity in sand in the principal planes of symmetry. The TE and TM modes along the z-axis are significantly affected by velocity dispersion.

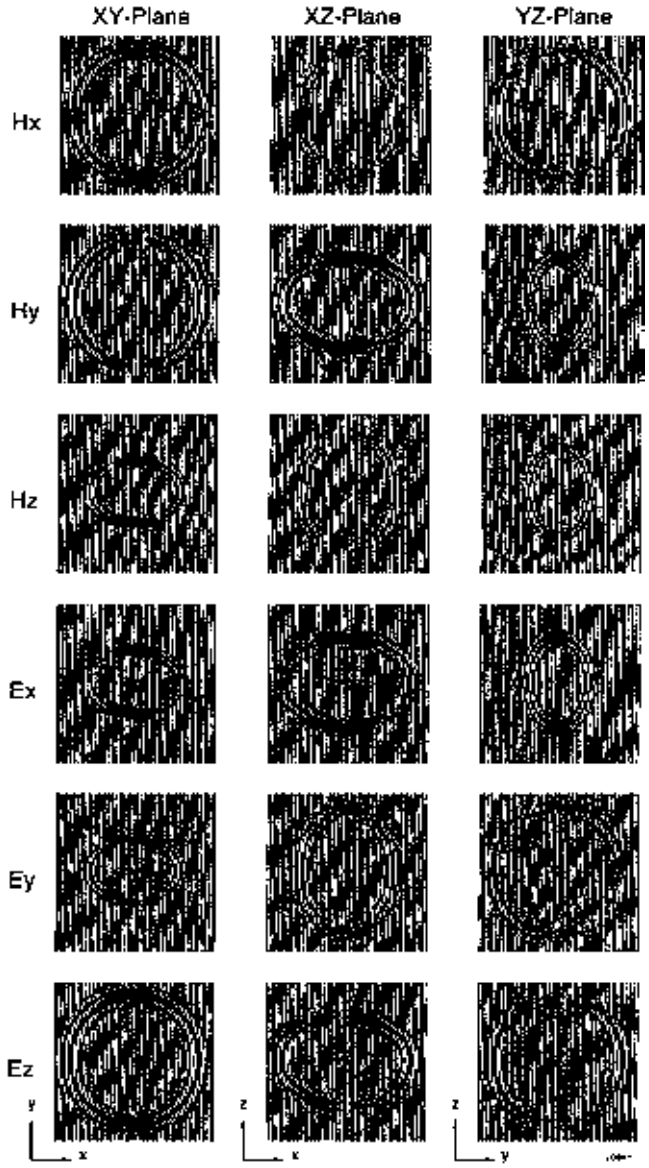

FIG. 5. Snapshots of the magnetic and electric fields at the coordinate planes (computed at 130 ns) for the medium defined in Table 1, including all loss mechanisms.

The number of grid points is the same as for the preceding example, the grid spacing is 2 cm, and the source is a y-directed electric dipole with a central frequency of 575 MHz [modeling a more general antenna radiation pattern requires the generalization to three dimensions of the 2-D method proposed by Carcione (1998)]. No free-surface effects are present since the purpose is to model propagation effects. The vertical grid points 5, 38, and 58 correspond to the antenna position, axial axes of the pipes, and sand–clay interface, respectively. The radiation pattern of the antenna, obtained with the simulation algorithm, is shown in Figure 9, where snapshots of the EM field are represented at the principal planes of the TI sand. Most of the energy is confined in the (x, y)- and (x, z)-planes, with little energy traveling downward. To avoid wraparound produced by the Fourier method, absorbing layers 20 grid points in length are implemented at the sides of the numerical mesh, with the upper absorbing layer located at the bottom of the mesh (Carcione, 1996c). The solution is computed with a time step of 0.02 ns.

Figure 10 shows snapshots of the H_x-component at an (x, z)-plane passing through the source location, where Figure 10a

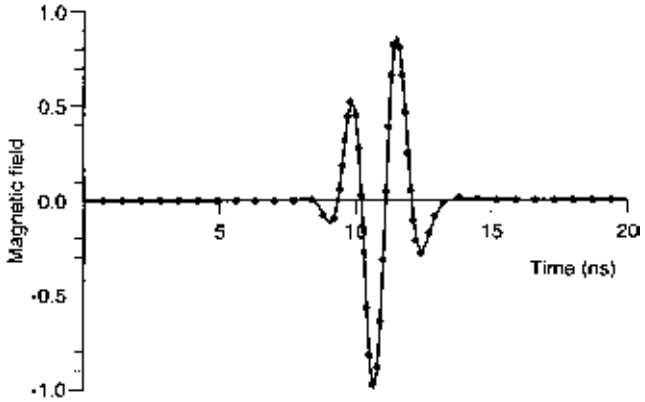

FIG. 6. Comparison between the numerical (dots) and analytical (continuos line) solutions corresponding to the horizontal component of the magnetic field.

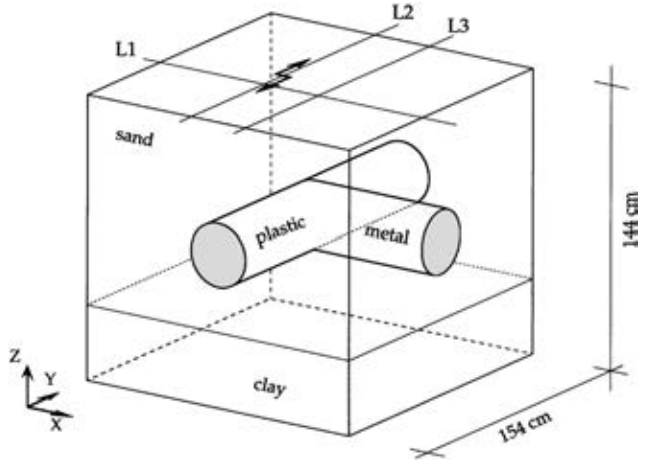

FIG. 7. Buried pipes in a finely stratified sand overlying a clay layer. The material properties are given in Table 2. The double arrow indicates the y-directed dipole antenna, and the receiver lines are denoted by L1, L2, and L3.

corresponds to the lossless and isotropic case and Figure 10b corresponds to the lossy anisotropic case (this snapshot is enhanced by a factor of 10). Isotropy is obtained by assuming that 33 components of the material tensors are equal to the corresponding 11 components. Besides the high dissipation, the field is delayed by velocity dispersion in Figure 10b (see Figure 8). Radargrams of the EM field have been computed at the three horizontal lines indicated in Figure 7 by labels L1, L2, and L3. They are shown in Figure 11 for the isotropic and lossless case, i.e., without dielectric relaxation and conductivity properties, and in Figure 12 for the lossy case. The scattered field from the pipes can be observed approximately between 15 and 25 ns, while the reflection from the sand–clay interface arrives after 30 ns. This event, which can be observed in the magnetic-field components, is relatively weak, since the dipole radiates little energy in the vertical direction. The amplitude and arrival times of all the events in Figure 12 are affected by attenuation, velocity dispersion, and anisotropy effects. For instance, the main event of the L2 radargram in Figure 11 arrives with an approximately 2-ns delay in the lossy case (Figure 12). The reverberations present in the lossless radargrams (generated in the pipes) are absent in Figure 12 because of the dissipation effects.

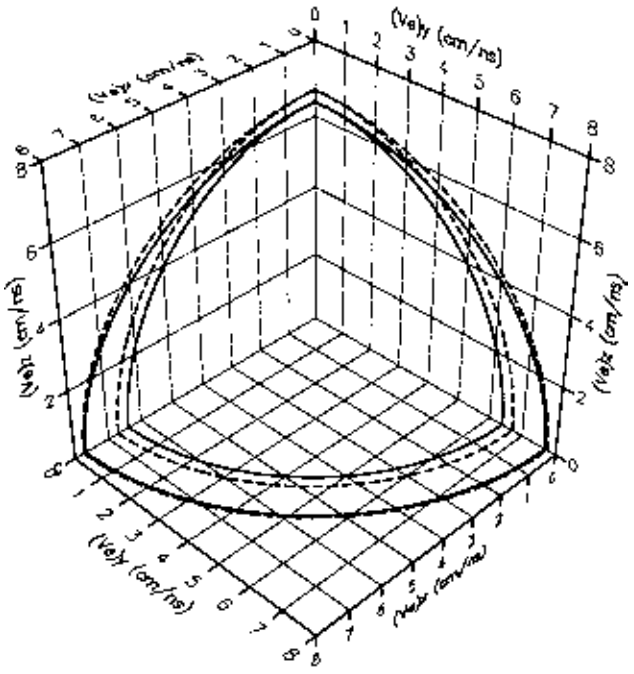

FIG. 8. Energy velocity curves at the principal planes of symmetry, corresponding to the sand indicated in Table 2. The solid line corresponds to a frequency of 1.15 GHz (the peak relaxation frequency), and the broken line corresponds to the lossless case. The TE mode corresponds to the inner curves in the vertical planes and the outer curve in the (x, y)-plane.

CONCLUSIONS

The proposed 3-D modeling technique uses a relaxation tensor formulation of material properties that accounts for

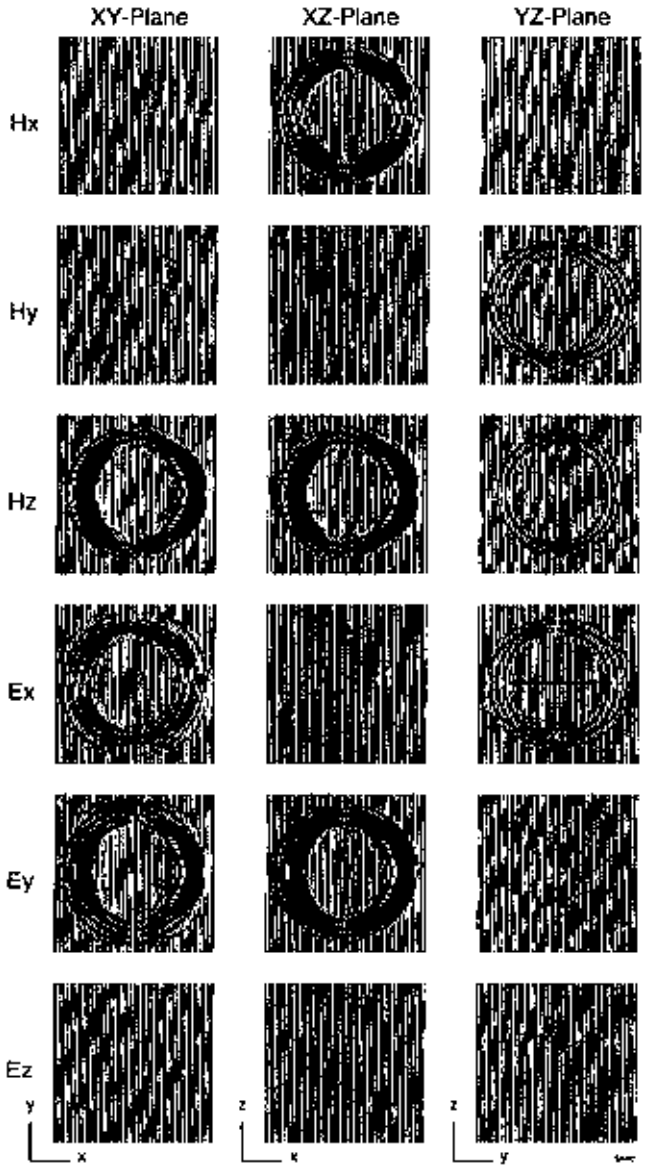

FIG. 9. Radiation pattern of a y-directed electric dipole at the principal planes of the TI sand whose properties are given in Table 2. Propagation time is 130 ns.

Table 2. Buried pipes in TI sand.

Medium	ϵ_1^∞ (ϵ_0)	ϵ_2^∞ (ϵ_0)	ϵ_3^∞ (ϵ_0)	Q_1^ϵ	Q_2^ϵ	Q_3^ϵ	σ_1^0 (S/m)	σ_2^0 (S/m)	σ_3^0 (S/m)
Sand	20	20	15	10	10	70	0.003	0.003	0.001
Clay	6	6	6	∞	∞	∞	0.01	0.01	0.01
Plastic	3	3	3	∞	∞	∞	0.0001	0.0001	0.0001
Metal	2	2	2	∞	∞	∞	0.5	0.5	0.5

$\epsilon_0 = 8.85\ 10^{-12}$ Fm^{-1}

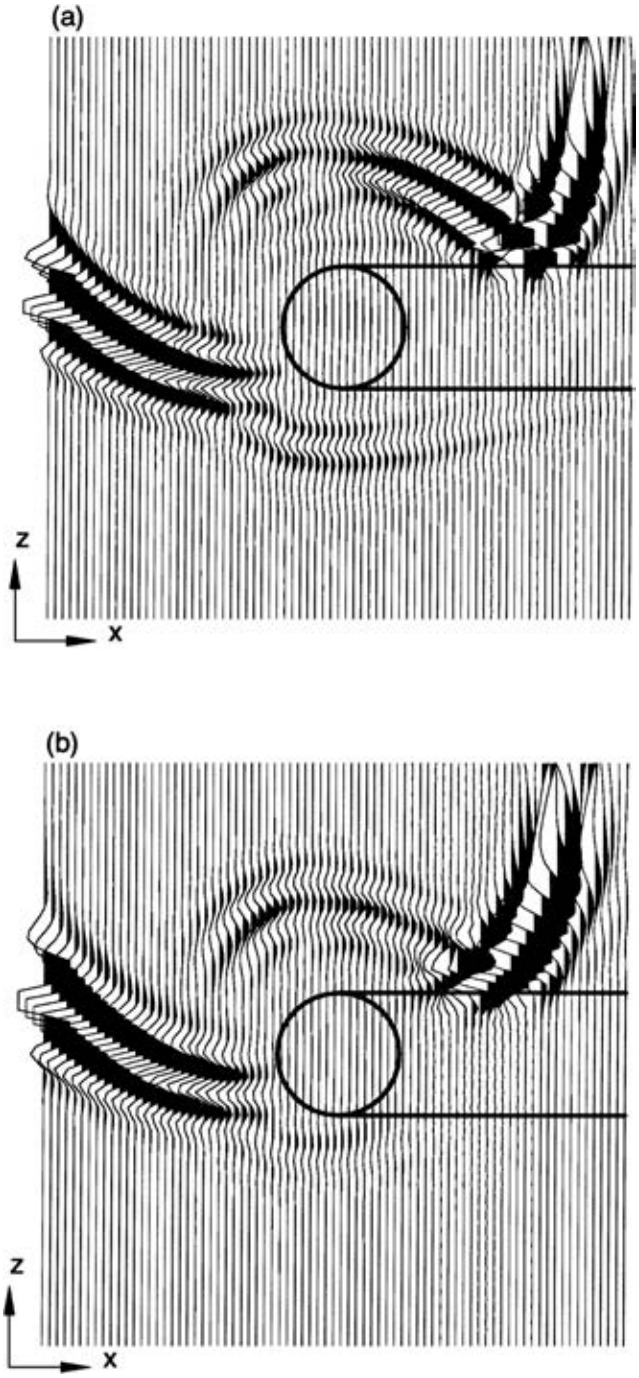

FIG. 10. Snapshots of the H_x-component at an (x, z)-plane passing through the source location, where (a) corresponds to the lossless and isotropic case and (b) corresponds to the lossy anisotropic case. (The second snapshot is enhanced by a factor 10.)

anisotropy and the various dissipation mechanisms in the radio frequency band. The Debye relaxations require the introduction of hidden variables whose differential equations are solved together with Maxwell's equations. A direct grid method solver, based on the Fourier differential operator and a staggered second-order time integration algorithm, allows the modeling of the complete wavefield.

A plane-wave analysis, based on uniform plane waves, gives the expression of measurable quantities, like quality factor and energy velocity. This analysis is fundamental for understanding the different wave phenomena when the medium is complex. For instance, in a TI medium, the TM curve in the isotropy plane and all the TE curves in the principal planes of symmetry are circles. On the other hand, for isotropic magnetic properties, the TM curves along planes containing the symmetry axis are ellipses in the lossless case and quasi-ellipses in the lossy case. Moreover, the anisotropic features of the attenuation factor (and quality factor) can differ substantially from those of the slowness and energy velocity surfaces. The modeling results are verified by plane-wave analysis and by comparison to a transient analyical solution.

In a GPR example, we compute radargrams corresponding to pipes buried in a finely stratified sand layer. Comparison between the ideal isotropic and lossless case and the anisotropic and lossy case indicates the importance of using a realistic modeling algorithm for GPR interpretation.

ACKNOWLEDGMENTS

This work was financed in part by the European Union under the INCO-COPERNICUS project Detection of Hydrocarbon Contaminated Soils by Electromagnetic Techniques, contract no. ERBIC15CT960801. We thank the reviewers and the associate editor for many comments and suggestions.

REFERENCES

Carcione, J. M., 1996a, Ground radar simulation for archaeological applications: Geophys. Prosp., **44**, 871–888.
——— 1996b, Ground-radar numerical modelling applied to engineering problems: Eur. J. Environ. Eng. Geophys., **1**, 65–81.
——— 1996c, Ground penetrating radar: wave theory and numerical simulation in lossy anisotropic media: Geophysics, **61**, 1664–1677.
——— 1998, Radiation patterns for GPR forward modeling: Geophysics, **63**, 424–430.
Carcione, J. M., Kosloff, D., Behle, A., and Seriani, G., 1992, A spectral scheme for wave propagation simulation in 3-D elastic-anisotropic media: Geophysics, **57**, 1593–1607.
Carcione, J. M., Kosloff, D., and Kosloff, R., 1988, Wave propagation in a linear viscoelastic medium: Geophys. J. Roy. Astr. Soc., **95**, 597–611.
Casper, D. A., and Kung, S., 1996, Simulation of ground-penetrating radar waves in a 2-D soil model: Geophysics, **61**, 1034–1049.
Casula, G., and Carcione, J. M., 1992, Generalized mechanical model analogies of linear viscoelastic behaviour: Boll. Geofis. Teor. Appl., **34**, 235–256.
Chew, W. C., 1990, Waves and fields in inhomogeneous media: Van Nostrand Reinhold, New York.
Fisher, E., McMechan, G. A., and Annan, P., 1992, Acquisition and processing of wide-aperture ground-penetrating radar data: Geophysics, **57**, 495–504.
Grandjean, G., and Gourry, J. C., 1996, GPR data processing for 3D fracture mapping in a marble quarry (Thassos, Greece): J. Appl. Geophys., **36**, 19–30.
Grasmueck, M., 1996, 3-D ground-penetrating radar applied to fracture imaging in gneiss: Geophysics, **61**, 1050–1064.
Hasted, J. B., 1973, Aqueous dielectrics: Chapman and Hall.
Hu, L. Z., 1992, Imaging pipelines in 3-D by ground-penetrating radar: 62nd Ann. Internat. Mtg., Soc. Expl. Geophys., Expanded Abstracts, 352–355.
Kosloff, D., and Baysal, E., 1982, Forward modeling by a Fourier method: Geophysics, **47**, 1402–1412.
Negi, J. G., and Saraf, P. D., 1989, Anisotropy in geoelectromagnetism: Elsevier Science Publ. Co., Inc.
Olhoeft, G. R., and Capron, D. E., 1994, Petrophysical causes of electromagnetic dispersion: Proc. Fifth Internat. Conf. on Ground Penetrating Radar, 145–152.
Petropoulos, P. G., 1995, The wave hierarchy for propagation in relaxing dielectrics: Wave Motion, **21**, 253–262.

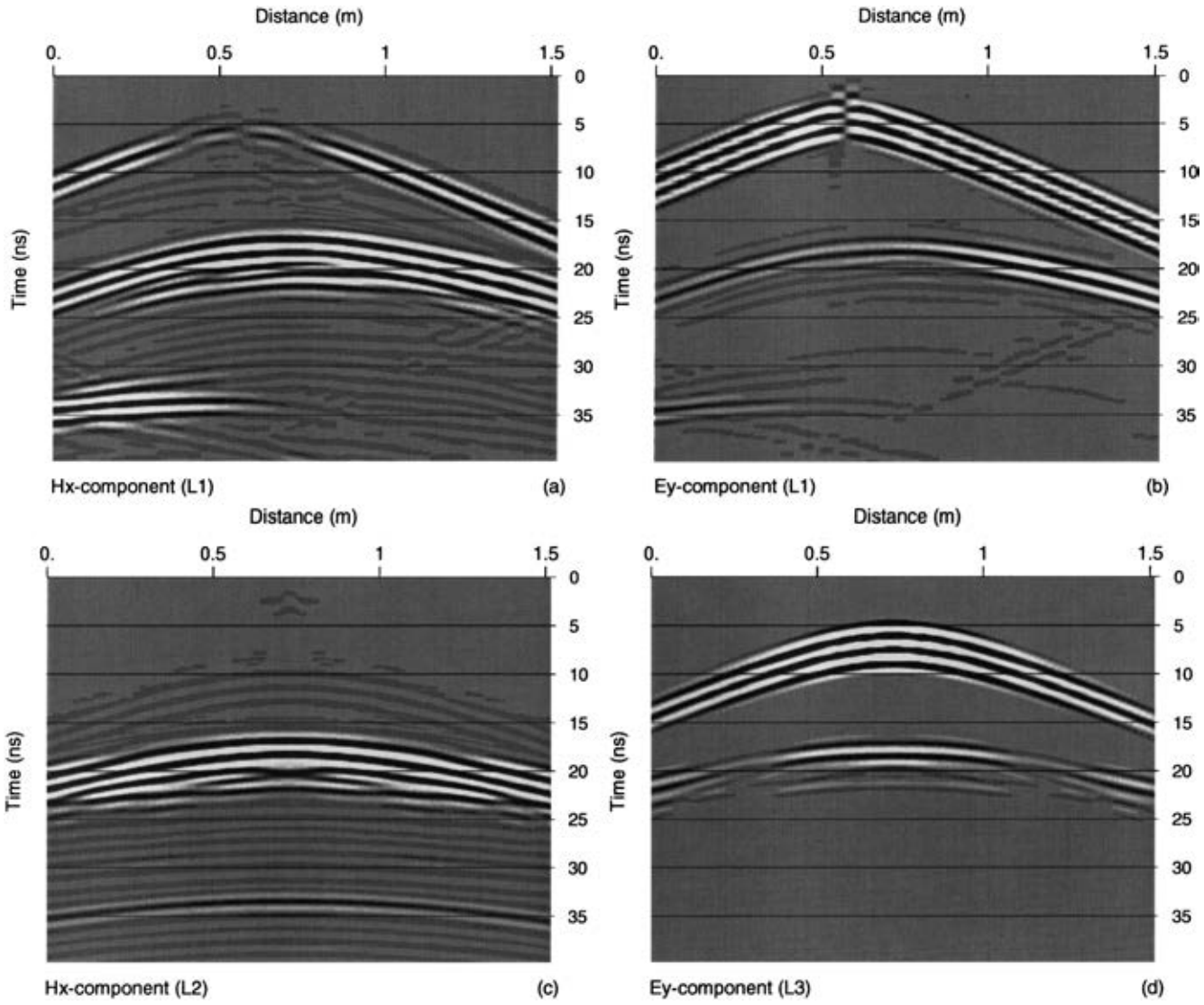

FIG. 11. Radargrams of the EM field computed at the three horizontal lines indicated in Figure 8. (a) and (b) The H_x- and E_y-components at line L1. (c) The H_x-component at line L2. (d) The E_y-component at line L3. They correspond to the isotropic and lossless case, i.e., without dielectric relaxation and conductivity properties.

Pipan, M., Finetti, I., and Ferigo, F., 1996, Multi-fold GPR techniques with applications to high-resolution studies: Two case histories: Eur. J. Environ. Eng. Geophys., **1**, 83–103.

Reshef, M., Kosloff, D., Edwards, M., and Hsiung, C., 1988a, Three-dimensional acoustic modeling by the Fourier method: Geophysics, **53**, 1175–1183.

——— 1988b, Three-dimensional elastic modeling by the Fourier method: Geophysics, **53**, 1184–1193.

Roberts, R. L., and Daniels, J. J., 1997, Modeling near-field GPR in three dimensions using the FDTD method: Geophysics, **62**, 1114–1126.

Schneider, J., and Hudson, S., 1993, The finite-difference time-domain method applied to anisotropic material: IEEE Trans. Antennas Propagat., **41**, 994–999.

Tillard, S., 1994, Radar experiments in isotropic and anisotropic geological formations (granite and schists): Geophys. Prosp., **42**, 615–636.

Walker, P., 1997, The importance of accounting for scattering by magnetic permeability contrasts: 59th Ann. Internat. Mtg., Eur. Assn. Expl. Geophys., Expanded Abstracts, F005.

Wang, T., and Tripp, A. C., 1994, Simulation of electromagnetic wave propagation in three-dimensional media by an FDTD method: Proc. Fifth Internat. Conf. on Ground Penetrating Radar, 247–267.

Xu, T., and McMechan, G. A., 1997, GPR attenuation and its numerical simulation in 2.5 dimensions: Geophysics, **62**, 403–414.

Zeng, X., McMechan, G. A., Cai, J., and Chen, H.-W., 1995, Comparison of ray and Fourier methods for modeling monostatic ground-penetrating radar profiles: Geophysics, **61**, 1727–1734.

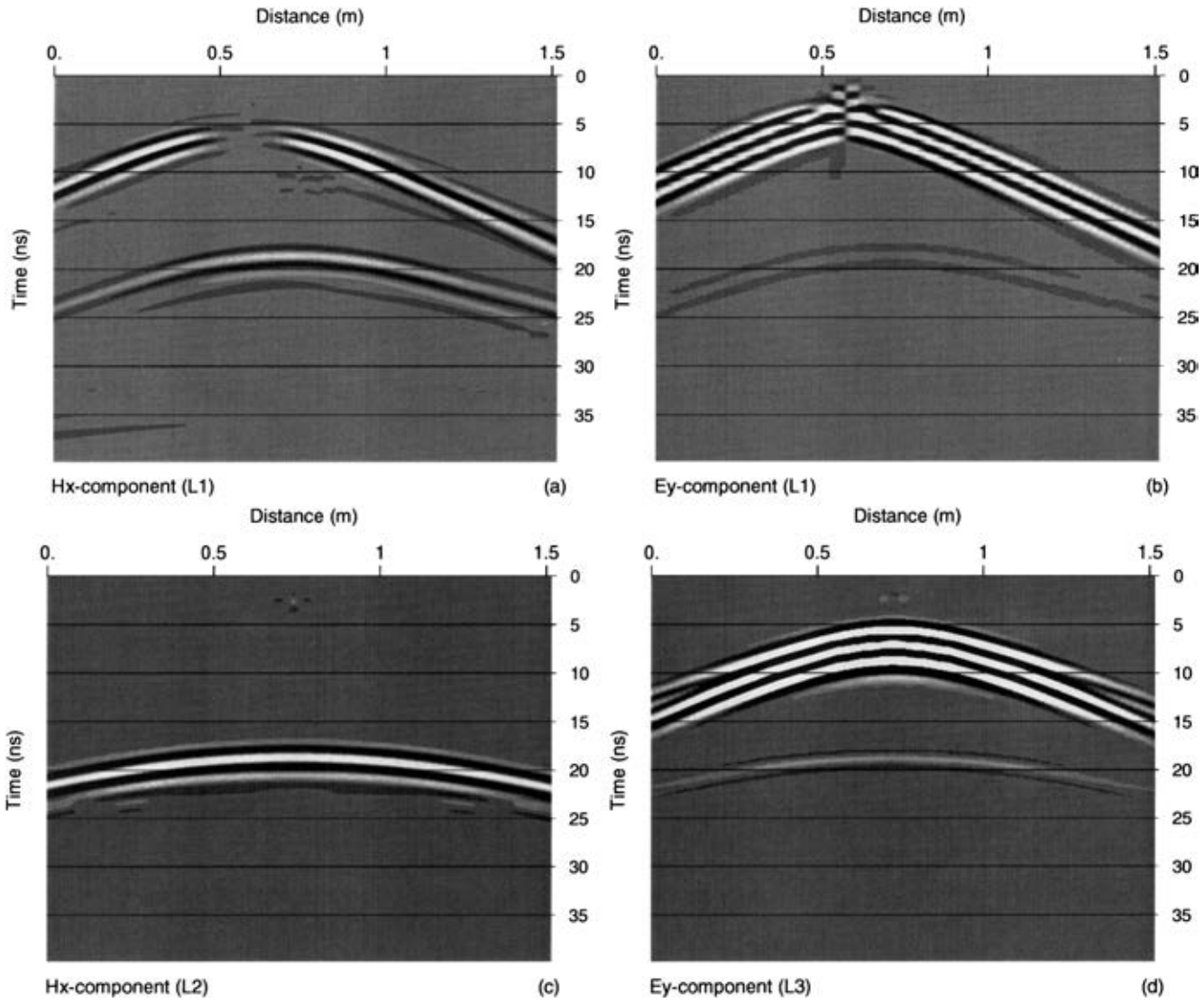

FIG. 12. Radargrams of the EM field for the model represented in Figure 8, including dielectric and conductivity losses.

APPENDIX A
PLANE-WAVE THEORY

Assume nonuniform harmonic plane waves with a phase factor

$$\exp[\imath\omega(\boldsymbol{\xi}\cdot\mathbf{x}-t)], \tag{A-1}$$

where $\boldsymbol{\xi}$, the complex slowness vector, is equivalent to $\mathbf{k}/\omega$, with $\mathbf{k}$ and ω being the wavenumber vector and frequency, respectively. The dot denotes the scalar product.

Note the following correspondences between time and frequency domain:

$$\nabla\times \rightarrow \imath\omega\boldsymbol{\xi}\times \quad \text{and} \quad \partial/\partial t \rightarrow -\imath\omega, \tag{A-2}$$

where $\times$ denotes the vector product.

Substituting the plane wave [equation (A-1)] into Maxwell's equations (4) in the absence of sources and using equation (A-2) gives

$$\boldsymbol{\xi}\times\mathbf{E} = \boldsymbol{\mu}\mathbf{H} \tag{A-3}$$

and

$$\boldsymbol{\xi}\times\mathbf{H} = -\bar{\boldsymbol{\epsilon}}\mathbf{E}, \tag{A-4}$$

where

$$\mathcal{F}\left(\frac{\partial\boldsymbol{\mu}}{\partial t}\right) \rightarrow \boldsymbol{\mu} \tag{A-5}$$

and

$$\mathcal{F}\left(\frac{\partial\boldsymbol{\epsilon}}{\partial t}\right) + \frac{\imath}{\omega}\mathcal{F}\left(\frac{\partial\boldsymbol{\sigma}}{\partial t}\right) \rightarrow \boldsymbol{\epsilon} + \frac{\imath}{\omega}\boldsymbol{\sigma} \equiv \bar{\boldsymbol{\epsilon}}. \tag{A-6}$$

The value $\mathcal{F}$ is the Fourier transform operator, using the $+\omega$ sign convention. For convenience, the medium properties are

denoted by the same symbols in both the time and frequency domains.

Note that $\bar{\epsilon}$ can be written alternatively as

$$\bar{\epsilon} = \epsilon_e + \frac{\imath}{\omega}\sigma_e, \tag{A-7}$$

where

$$\epsilon_e = \mathrm{Re}(\epsilon) - \frac{1}{\omega}\,\mathrm{Im}(\sigma) \tag{A-8}$$

and

$$\sigma_e = \mathrm{Re}(\sigma) + \omega\,\mathrm{Im}(\epsilon) \tag{A-9}$$

are the real effective permittivity and conductivity matrices, respectively, and where the operators $\mathrm{Re}(\cdot)$ and $\mathrm{Im}(\cdot)$ take the real and imaginary part, respectively.

The components of ϵ and σ from equations (7) and (10) are

$$\epsilon_i = \mathcal{F}\left[\frac{\partial \epsilon_i}{\partial t}\right] = \frac{\epsilon_i^0}{L_i}\sum_{\ell=1}^{L_i}\frac{1-\imath\omega\lambda_{i\ell}}{1-\imath\omega\tau_{i\ell}} \tag{A-10}$$

and

$$\sigma_i = \mathcal{F}\left[\frac{\partial \sigma_i}{\partial t}\right] = \sigma_i^0(1-\imath\omega\chi_i). \tag{A-11}$$

The permittivity component (A-10) can be rewritten in a more familiar way as

$$\epsilon_i = \epsilon_i^\infty + \frac{1}{L_i}\sum_{\ell=1}^{L_i}\frac{\epsilon_i^0-\epsilon_{i\ell}^\infty}{1-\imath\omega\tau_{i\ell}}, \tag{A-12}$$

where $\epsilon_{i\ell}^\infty = \epsilon_i^0\lambda_{i\ell}/\tau_{i\ell}$ is the infinite-frequency permittivity of the ℓth relaxation mechanism. A similar expression is used in bioelectromagnetics (Petropoulos, 1995).

Similarly, from equation (9),

$$\mu_i = \mathcal{F}\left[\frac{\partial \mu_i}{\partial t}\right] = \frac{\mu_i^0}{N_i}\sum_{n=1}^{N_i}\frac{1-\imath\omega\gamma_{in}}{1-\imath\omega\theta_{in}}. \tag{A-13}$$

Since $\lambda_{i\ell} \le \tau_{i\ell}$ implies $\mathrm{Im}(\tilde{\epsilon}_i) \ge 0$ and $\mathrm{Re}(\tilde{\sigma}_i) \ge 0$, the two terms on the right side of equation (A-9) have the same sign and the wave process is always dissipative. The importance of the effective matrices is that their components are the quantities measured in laboratory experiments: ϵ_e produces a current out of phase with the electric field, while σ_e produces a current that varies in phase with the electric field. The coefficients multiplying the electric field and the time derivative of the electric field in equations (15) correspond to the components of σ_e^∞ and ϵ_e^∞, respectively.

Taking the vector product of equation (A-3) with $\boldsymbol{\xi}$ gives

$$\boldsymbol{\xi}\times(\boldsymbol{\mu}^{-1}\boldsymbol{\xi}\times\mathbf{E}) = \boldsymbol{\xi}\times\mathbf{H}, \tag{A-14}$$

which, with equation (A-4), becomes

$$\boldsymbol{\xi}\times(\boldsymbol{\mu}^{-1}\boldsymbol{\xi}\times\mathbf{E}) + \bar{\epsilon}\mathbf{E} = 0 \tag{A-15}$$

for three equations for the components of $\mathbf{E}$. Alternatively, the vector product of equation (A-4) with $\boldsymbol{\xi}$ and use of equation (A-3) yields

$$\boldsymbol{\xi}\times[(\bar{\epsilon})^{-1}\boldsymbol{\xi}\times\mathbf{H}] + \boldsymbol{\mu}\mathbf{H} = 0 \tag{A-16}$$

for three equations for the components of $\mathbf{H}$.

The equivalent of the 3×3 viscoelastic Christoffel equations for the electric field vector components are

$$\left(e_{ijk}\xi_j\mu_{k\ell}^{-1}e_{\ell pq}\xi_p + \bar{\epsilon}_{iq}\right)E_q = 0, \tag{A-17}$$

where the subindices take the values 1, 2, and 3 and where e_{ijk} are the elements of the Levi-Civita tensor.

Similarly, the equations for the magnetic field vector components are

$$\left(e_{ijk}\xi_j(\bar{\epsilon}_{k\ell})^{-1}e_{\ell pq}\xi_p + \mu_{iq}\right)H_q = 0. \tag{A-18}$$

Both dispersion relations (A-17) and (A-18) are identical. Getting one relation from the other implies an interchange of ϵ_i and μ_i, and vice versa.

So far, the dispersion relations correspond to a general triclinic medium. Consider the orthorhombic case given by equations (5). Then, the analog of the Christoffel equation for the electric field vector is

$$\boldsymbol{\Gamma}\mathbf{E} = \mathbf{0}, \tag{A-19}$$

where the EM Christoffel matrix is

$$\boldsymbol{\Gamma} = \begin{pmatrix} \bar{\epsilon}_1 - \left(\dfrac{\xi_2^2}{\mu_3}+\dfrac{\xi_3^2}{\mu_2}\right) & \dfrac{\xi_1\xi_2}{\mu_3} & \dfrac{\xi_1\xi_3}{\mu_2} \\ \dfrac{\xi_1\xi_2}{\mu_3} & \bar{\epsilon}_2 - \left(\dfrac{\xi_1^2}{\mu_3}+\dfrac{\xi_3^2}{\mu_1}\right) & \dfrac{\xi_2\xi_3}{\mu_1} \\ \dfrac{\xi_1\xi_3}{\mu_2} & \dfrac{\xi_2\xi_3}{\mu_1} & \bar{\epsilon}_3 - \left(\dfrac{\xi_1^2}{\mu_2}+\dfrac{\xi_2^2}{\mu_1}\right) \end{pmatrix}. \tag{A-20}$$

After defining

$$\eta_i = \epsilon_i\mu_i, \quad \zeta_i = \epsilon_j\mu_k + \epsilon_k\mu_j, \quad j\ne k\ne i, \tag{A-21}$$

the 3-D dispersion relation (i.e., the vanishing of the determinant of the Christoffel matrix) becomes

$$\begin{aligned}&\left(\bar{\epsilon}_1\xi_1^2 + \bar{\epsilon}_2\xi_2^2 + \bar{\epsilon}_3\xi_3^2\right)\left(\mu_1\xi_1^2 + \mu_2\xi_2^2 + \mu_3\xi_3^2\right)\\ &\quad - \left(\eta_1\zeta_1\xi_1^2 + \eta_2\zeta_2\xi_2^2 + \eta_3\zeta_3\xi_3^2\right) + \eta_1\eta_2\eta_3 = 0.\end{aligned} \tag{A-22}$$

As stated in the first section, there are only quartic and quadratic terms of the slowness components in the dispersion relation of an orthorhombic medium.

Slowness, phase velocity, and attenuation

The slowness vector can be split into real and imaginary vectors such that $\omega\,\mathrm{Re}(\boldsymbol{\xi}\cdot\mathbf{x}-t)$ is the phase and $-\omega\,\mathrm{Im}(\boldsymbol{\xi}\cdot\mathbf{x})$ is the attenuation. Assume that propagation and attenuation directions coincide to produce a uniform plane wave, which is equivalent to a homogeneous plane wave in viscoelasticity. The slowness vector can be expressed as

$$\boldsymbol{\xi}=\xi(\ell_1,\ell_2,\ell_3)^{\top}\equiv\xi\hat{\boldsymbol{\xi}}, \tag{A-23}$$

where ξ is the complex slowness and $\hat{\boldsymbol{\xi}}=(\ell_1,\ell_2,\ell_3)^{\top}$ is a real unit vector, with ℓ_i the direction cosines. We obtain the real wavenumber vector and the real attenuation vector as

$$\mathrm{Re}(\boldsymbol{\xi})\qquad\text{and}\qquad\boldsymbol{\alpha}=\omega\,\mathrm{Im}(\boldsymbol{\xi}), \tag{A-24}$$

respectively.

Substituting equation (A-23) into the dispersion relation (A-22) yields

$$A\xi^4-B\xi^2+\eta_1\eta_2\eta_3=0, \tag{A-25}$$

where

$$A=\left(\bar{\epsilon}_1\ell_1^2+\bar{\epsilon}_2\ell_2^2+\bar{\epsilon}_3\ell_3^2\right)\left(\mu_1\ell_1^2+\mu_2\ell_2^2+\mu_3\ell_3^2\right)$$

and

$$B=\eta_1\zeta_1\ell_1^2+\eta_2\zeta_2\ell_2^2+\eta_3\zeta_3\ell_3^2.$$

In terms of the complex velocity $V\equiv\xi^{-1}$, the phase velocity and attenuation are

$$V_p=[\mathrm{Re}(V^{-1})]^{-1}\qquad\text{and}\qquad\alpha=\omega\,\mathrm{Im}(V^{-1}), \tag{A-26}$$

respectively.

Assume, for instance, propagation in the (1, 2)-plane. Then, $\ell_3=0$ and the dispersion relation (A-25) is factorizable, giving

$$\left[\xi^2\left(\bar{\epsilon}_1\ell_1^2+\bar{\epsilon}_2\ell_2^2\right)-\bar{\epsilon}_1\bar{\epsilon}_2\mu_3\right]\times\left[\xi^2\left(\mu_1\ell_1^2+\mu_2\ell_2^2\right)-\bar{\epsilon}_3\mu_1\mu_2\right]=0. \tag{A-27}$$

These factors give the TM and TE modes with complex velocities

$$V^{\mathrm{TM}}=\left(\frac{\ell_1^2}{\bar{\epsilon}_2\mu_3}+\frac{\ell_2^2}{\bar{\epsilon}_1\mu_3}\right)^{1/2}$$

and (A-28)

$$V^{\mathrm{TE}}=\left(\frac{\ell_1^2}{\mu_2\bar{\epsilon}_3}+\frac{\ell_2^2}{\mu_1\bar{\epsilon}_3}\right)^{1/2}.$$

In the TM (TE) case the magnetic (electric) field vector is perpendicular to the propagation plane. For obtaining the slowness and complex velocities for the other planes, make the following subindex substitutions:

from the (1, 2)-plane to the (1, 3)-plane

$(1,2,3)\rightarrow(3,1,2)$;

from the (1, 2)-plane to the (2, 3)-plane (A-29)

$(1,2,3)\rightarrow(2,3,1)$.

The analysis of all three planes of symmetry gives the slowness sections represented in Figure A-1, where the values on the axes refer to the square of the complex slowness (in particular, the curves correspond to the material defined in Table 1). There exists a single conical point given by the intersection of the TE and TM modes, as can be seen in the (1, 3)-plane of symmetry. The location of the conical point depends on the values of the material properties.

Energy velocity and quality factor

The scalar product of the complex conjugate of equation (A-4) with $\mathbf{E}$, use of the relation $2\,\mathrm{Im}(\boldsymbol{\xi})\cdot(\mathbf{E}\times\mathbf{H}^*)=(\boldsymbol{\xi}\times\mathbf{E})\cdot\mathbf{H}^*+\mathbf{E}\cdot(\boldsymbol{\xi}\times\mathbf{H})^*$, and substitution of equation (A-3) gives the Umov–Poynting theorem for plane waves:

$$\mathrm{Im}(\boldsymbol{\xi})\cdot\mathbf{P}=\imath(u_e-u_m), \tag{A-30}$$

where

$$\mathbf{P}=\frac{1}{2}\mathbf{E}\times\mathbf{H}^* \tag{A-31}$$

is the complex Umov-Poynting vector and

$$u_e=\frac{1}{4}\mathbf{E}\cdot(\bar{\boldsymbol{\epsilon}}\mathbf{E})^*,\qquad u_m=\frac{1}{4}(\boldsymbol{\mu}\mathbf{H})\cdot\mathbf{H}^* \tag{A-32}$$

are the complex time average electric and magnetic energy densities, respectively. The imaginary part of equation (A-30) gives the balance of stored energy, and the real part gives the balance of dissipated energy.

The energy velocity vector ($\mathbf{V}_e$) is given by the energy power flow $\mathbf{P}_R\equiv\mathrm{Re}(\mathbf{P})$ divided by the total stored energy density, so $u_s\equiv\mathrm{Re}(u_e+u_m)$:

$$\mathbf{V}_e=\frac{\mathrm{Re}(\mathbf{P})}{\mathrm{Re}(u_e+u_m)}. \tag{A-33}$$

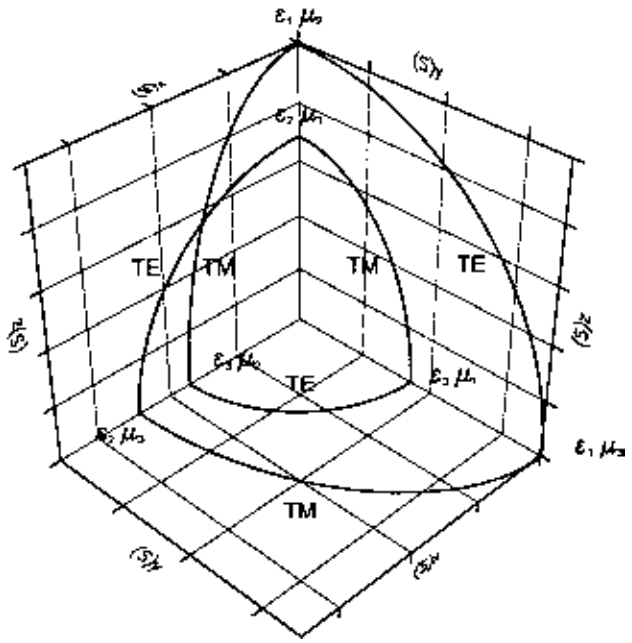

FIG. A-1. Intersection of the slowness surface with the principal planes. The corresponding waves are either transverse electric (TE) or transverse magnetic (TM). The values at the axes refer to the square of the complex slowness.

We define the quality factor (Q) as the total energy density divided by twice the total dissipated energy density $u_d \equiv \mathrm{Im}(u_m - u_e)$, so

$$Q = \frac{u_s}{2u_d}. \tag{A-34}$$

This definition of quality factor differs from the standard definition in that it is based solely on the electric energy density. With an $\exp(\imath\omega t)$ dependence, the dissipated energy is given by $\mathrm{Im}(u_e - u_m)$.

Consider the TE mode propagating in the $(1,2)$-plane. Then,

$$\mathbf{E} = E_0[0,0,1]^\top \exp[\imath(\boldsymbol{\xi}\cdot\mathbf{x})], \tag{A-35}$$

where E_0 is a complex amplitude. By equation (2),

$$\mathbf{H} = \boldsymbol{\mu}^{-1}\boldsymbol{\xi}\times\mathbf{E} = E_0\xi\left[\frac{\ell_2}{\mu_1}, -\frac{\ell_1}{\mu_2}, 0\right]^\top \exp[\imath(\boldsymbol{\xi}\cdot\mathbf{x})], \tag{A-36}$$

where we assume uniform plane waves. Substituting the electric and magnetic fields into the energy densities (A-32) yields

$$\begin{aligned} u_e^{\mathrm{TE}} &= \frac{1}{4}\bar{\epsilon}_3^*|E_0|^2\exp(-2\boldsymbol{\alpha}\cdot\mathbf{x}),\\ u_m^{\mathrm{TE}} &= \frac{1}{4}|E_0|^2\frac{\left(\bar{\epsilon}_3V^2\right)^*}{|V|^2}\exp(-2\boldsymbol{\alpha}\cdot\mathbf{x}), \end{aligned} \tag{A-37}$$

where the complex velocity $V=\xi^{-1}$ and the attenuation $\boldsymbol{\alpha}$ is given by equation (A-26). Summing the electric and magnetic energies and taking real part gives the total stored energy

$$u_s^{\mathrm{TE}} = \frac{1}{2}|E_0|^2\,\mathrm{Re}\left(\bar{\epsilon}_3\frac{V}{V_p}\right)\exp(-2\boldsymbol{\alpha}\cdot\mathbf{x}), \tag{A-38}$$

where V_p is the phase velocity [equation (A-26)]. The TE power flow vector is

$$\mathbf{P}_R^{\mathrm{TE}} = \frac{1}{2}|E_0|^2\,\mathrm{Re}\left[\frac{1}{V^*}\left(\hat{\mathbf{e}}_1\frac{\ell_1}{\mu_2^*}+\hat{\mathbf{e}}_2\frac{\ell_2}{\mu_1^*}\right)\right]\exp(-2\boldsymbol{\alpha}\cdot\mathbf{x}). \tag{A-39}$$

From equations (A-37) and (A-39) we obtain the energy velocity for TE waves propagating in the $(1,2)$-plane as

$$\mathbf{V}_e^{\mathrm{TE}} = \frac{V_p}{\mathrm{Re}(\bar{\epsilon}_3V)}\left[\ell_1\,\mathrm{Re}\left(\frac{1}{V\mu_2}\right)\hat{\mathbf{e}}_1+\ell_2\,\mathrm{Re}\left(\frac{1}{V\mu_1}\right)\hat{\mathbf{e}}_2\right]. \tag{A-40}$$

Performing similar calculations, the energy densities, power flow vector, and energy velocity for TM waves propagating in the $(1,2)$-plane are

$$\begin{aligned} u_e^{\mathrm{TM}} &= \frac{1}{4}|H_0|^2\frac{\mu_3V^2}{|V|^2}\exp(-2\boldsymbol{\alpha}\cdot\mathbf{x}),\\ u_m^{\mathrm{TM}} &= \frac{1}{4}\mu_3|H_0|^2\exp(-2\boldsymbol{\alpha}\cdot\mathbf{x}), \end{aligned} \tag{A-41}$$

$$u_s^{\mathrm{TM}} = \frac{1}{2}|H_0|^2\,\mathrm{Re}\left[\mu_3\frac{V}{V_p}\right]\exp(-2\boldsymbol{\alpha}\cdot\mathbf{x}), \tag{A-42}$$

$$\mathbf{P}_R^{\mathrm{TM}} = \frac{1}{2}|H_0|^2\,\mathrm{Re}\left[\frac{1}{V}\left(\hat{\mathbf{e}}_1\frac{\ell_1}{\bar{\epsilon}_2}+\hat{\mathbf{e}}_2\frac{\ell_2}{\bar{\epsilon}_1}\right)\right]\exp(-2\boldsymbol{\alpha}\cdot\mathbf{x}), \tag{A-43}$$

and

$$\mathbf{V}_e^{\mathrm{TM}} = \frac{V_p}{\mathrm{Re}(\mu_3V)}\left[\ell_1\,\mathrm{Re}\left(\frac{1}{V\bar{\epsilon}_2}\right)\hat{\mathbf{e}}_1+\ell_2\,\mathrm{Re}\left(\frac{1}{V\bar{\epsilon}_1}\right)\hat{\mathbf{e}}_2\right]. \tag{A-44}$$

Calculation of the dissipated energy for TE and TM waves yields

$$u_d^{\mathrm{TE}} = \frac{1}{2}|E_0|^2\,\mathrm{Re}\left[\bar{\epsilon}_3\frac{\alpha V}{\omega}\right]\exp(-2\boldsymbol{\alpha}\cdot\mathbf{x}) \tag{A-45}$$

and

$$u_d^{\mathrm{TM}} = \frac{1}{2}|H_0|^2\,\mathrm{Re}\left[\mu_3\frac{\alpha V}{\omega}\right]\exp(-2\boldsymbol{\alpha}\cdot\mathbf{x}), \tag{A-46}$$

respectively. Then, using equations (A-38) and (A-42), the quality factor (A-34) takes the simple form

$$Q = \frac{\omega}{2\alpha V_p}. \tag{A-47}$$

The form (A-47) coincides with the relation between quality factor and attenuation for low-loss viscoelastic media, although we do not invoke such a restriction. This difference is due to different definitions. In viscoelasticity, the Q factor commonly is defined in terms of the mean strain energy; here, it is defined in terms of half the total energy.

Alternative definitions of the quality factor that distinguish between electric and magnetic losses are

$$Q_e = -\frac{\mathrm{Re}(u_e)}{\mathrm{Im}(u_e)}, \qquad Q_m = \frac{\mathrm{Re}(u_m)}{\mathrm{Im}(u_m)}, \tag{A-48}$$

giving

$$\begin{aligned} Q_e^{\mathrm{TE}} &= \frac{\mathrm{Re}(\bar{\epsilon}_3)}{\mathrm{Im}(\bar{\epsilon}_3)}, \qquad Q_e^{\mathrm{TM}} = -\frac{\mathrm{Re}\left(\mu_3V^2\right)}{\mathrm{Im}\left(\mu_3V^2\right)}\\ \text{and}\\ Q_m^{\mathrm{TE}} &= -\frac{\mathrm{Re}\left(\bar{\epsilon}_3V^2\right)}{\mathrm{Im}\left(\bar{\epsilon}_3V^2\right)}, \qquad Q_m^{\mathrm{TM}} = \frac{\mathrm{Re}(\mu_3)}{\mathrm{Im}(\mu_3)}. \end{aligned} \tag{A-49}$$

The expressions of the energy velocities and quality factors corresponding to the $(1,3)$- and $(2,3)$-planes can be obtained by making the substitutions (A-29).

APPENDIX B
TIME INTEGRATION TECHNIQUE

Spatial derivatives are calculated with the Fourier method by using the fast Fourier transform (FFT). This approximation, used also in the 2-D case (Carcione, 1996c), is infinitely accurate for band-limited periodic functions with spatial wavenumbers which are smaller than the Nyquist wavenumbers of the mesh.

Let us define the central differences and mean value operators

$$D^j\xi = \frac{\xi^{n+j} - \xi^{n+j-1}}{dt} \quad \text{and} \quad A^j\xi = \frac{\xi^{n+j} + \xi^{n+j-1}}{2},$$

where dt is the time step and $j = 0, 1/2$, or 1. Assume the x_1-component and one hidden variable. We start with the semistaggered vector

$$[H^{n-1/2}, E^n, e^{n-1/2}, d^n]^\top$$

for each field component and obtain

$$[H^{n+1/2}, E^{n+1}, e^{n+1/2}, d^{n+1}]^\top.$$

For the procedure, first compute

$$\left(\frac{\partial E_2}{\partial x_3} - \frac{\partial E_3}{\partial x_2}\right)^n$$

in equation (15). Second, compute $H_1^{n+1/2}$ using equation (15) discretized at time ndt:

$$\left(\frac{\partial E_2}{\partial x_3} - \frac{\partial E_3}{\partial x_2}\right)^n = \mu_1^\infty D^{1/2} H_1 + \mu_1^0\left[\Psi_1 A^{1/2} H_1 + d_1^n\right] + M_1^n.$$

Third, compute $e_1^{n+1/2}$ from equation (19) discretized at ndt:

$$D^{1/2} e_1 = -\frac{1}{\tau_1}\left[A^{1/2} e_1 + \phi_1(0) E_1^n\right].$$

Fourth, compute d_1^{n+1} from equation (19) discretized at $(n + 1/2)dt$:

$$D^1 d_1 = -\frac{1}{\theta_1}\left[A^1 d_1 + \varphi_1(0) H_1^{n+1/2}\right].$$

Fifth, compute

$$\left(\frac{\partial H_3}{\partial x_2} - \frac{\partial H_2}{\partial x_3}\right)^{n+1/2}$$

in equation (15). Finally, compute E_1^{n+1} from equation (15) discretized at time $(n + 1/2)dt$:

$$\left(\frac{\partial H_3}{\partial x_2} - \frac{\partial H_2}{\partial x_3}\right)^{n+1/2} = \sigma_{e1}^\infty A^1 E_1 + \epsilon_{e1}^\infty D^1 E_1 + \epsilon_1^0 e_1^{n+1/2} + J_1^{n+1/2}.$$

The presence of nonzero off-diagonal elements in the permittivity and conductivity tensors does not require any interpolation as in the Yee algorithm (Schneider and Hudson, 1993).